Nanoscale Horizons

ROYAL SOCIETY OF CHEMISTRY

COMMUNICATION

View Article Online
View Journal | View Issue

Cite this: *Nanoscale Horiz.*, 2024, 9, 1514

Received 29th May 2024,
Accepted 20th June 2024

DOI: 10.1039/d4nh00243a

rsc.li/nanoscale-horizons

An ionically cross-linked composite hydrogel electrolyte based on natural biomacromolecules for sustainable zinc-ion batteries†

Haoyang Ge,[a] Liping Qin,*[b] Bingyao Zhang,[a] Long Jiang,[c] Yan Tang,[a] Bingan Lu,[d] Siyu Tian*[a] and Jiang Zhou*[a]

Zinc-ion batteries (ZIBs) are regarded as promising power sources for flexible and biocompatible devices due to their good sustainability and high intrinsic safety. However, their applications have been hindered by the issues of uncontrolled Zn dendrite growth and severe water-induced side reactions in conventional liquid electrolytes. Herein, an ionically cross-linked composite hydrogel electrolyte based on natural biomacromolecules, including iota-carrageenan and sodium alginate, is designed to promote highly efficient and reversible Zn plating/stripping. The abundant functional groups of macromolecules effectively suppress the reactivity of water molecules and facilitate uniform Zn deposition. Moreover, the composite hydrogel electrolyte exhibits a high ionic conductivity of 5.89×10^{-2} S cm^{-1} and a Zn^{2+} transference number of 0.58. Consequently, the Zn‖Zn symmetric cell with the composite hydrogel electrolyte shows a stable cycle life of more than 500 h. Meanwhile, the Zn‖$NH_4V_4O_{10}$ coin cell with the composite hydrogel electrolyte retains a high specific capacity of approximately 200 mA h g^{-1} after 600 cycles at 2 A g^{-1}. The Zn‖NVO pouch cell based on the composite hydrogel electrolyte also shows a high specific capacity of 246.1 mA h g^{-1} at 0.5 A g^{-1} and retains 70.7% of its initial capacity after 150 cycles. The pouch cell performs well at different bending angles and exhibits a capacity retention rate of 98% after returning to its initial state from 180° folding. This work aims to construct high-performance hydrogel electrolytes using low-cost natural materials, which may provide a solution for the application of ZIBs in flexible biocompatible devices.

New concepts

Zinc-ion batteries based on aqueous electrolytes and a Zn anode are potential candidates for the power supply in safe and biocompatible electronics. However, the thermodynamic instability and poor reversibility of the Zn anode in conventional zinc sulfate–base aqueous electrolytes remain a significant challenge. In this work, a novel composite hydrogel electrolyte composed of graphene oxide and low-cost natural biomacromolecules, including sodium alginate and iota-carrageenan, was designed. The double-networked hydrogel framework was ionically cross-linked by Zn^{2+}, and the introduction of graphene oxide facilitated fast Zn^{2+} transport within the composite hydrogel electrolyte. More importantly, the biomacromolecules formed strong hydrogen bonds with water molecules and homogenized Zn^{2+} distributions, enabling a highly reversible Zn anode in aqueous environments. This work highlights the potential of biomacromolecules in developing biocompatible and safe zinc-ion batteries.

1. Introduction

Zinc-ion batteries (ZIBs) are promising energy storage systems for the power supply of biocompatible devices. Compared to lithium-ion batteries, ZIBs based on a Zn anode and aqueous electrolytes exhibit high safety and low toxicity. Moreover, the Zn anode exhibits a high theoretical capacity (820 mA h g^{-1}) and a low redox potential (−0.763 V *vs.* a standard hydrogen electrode), making ZIBs competitive for high-performance, biocompatible energy storage systems.[1,2] Unfortunately, ZIBs face problems associated with the Zn anode and aqueous electrolytes, such as dendrite formation and water-induced side reactions, resulting in unsatisfactory performance and service life.[3–6] To address these challenges, several electrolyte systems have been widely explored, including aqueous/organic hybrid electrolytes, hydrogel electrolytes, and "water-in-salt" electrolytes.[7–9] Among them, hydrogel electrolytes based on polymeric materials exhibit substantial

---

[a] School of Materials Science and Engineering, Hunan Provincial Key Laboratory of Electronic Packaging and Advanced Functional Materials, Central South University, Changsha 410083, China. E-mail: sytian2016@163.com, zhou_jiang@csu.edu.cn

[b] College of Biological and Chemical Engineering, Guangxi University of Science and Technology, Liuzhou 545006, Guangxi, China. E-mail: qinlp2005@126.com

[c] State Key Laboratory of Oil and Gas Equipment, CNPC Tubular Goods Research Institute, Xi'an 710077, China

[d] School of Physics and Electronics, Hunan University, Changsha 410082, China

† Electronic supplementary information (ESI) available. See DOI: https://doi.org/10.1039/d4nh00243a

potential for biocompatible applications due to their extraordinary physicochemical properties.[10–12] Meanwhile, the presence of hydrophilic functional groups in the polymers is advantageous in inhibiting parasitic water-induced side reactions and thus facilitating reversible Zn plating/stripping in aqueous environments.[13,14]

To date, several polymeric materials have been widely used as the frameworks of hydrogel electrolytes, including polyacrylamide, polyvinyl alcohol, gelatin, alginate, chitosan, agarose and cellulose.[15,16] However, the biocompatibility of the hydrogel electrolytes based on synthetic polymers (*e.g.*, polyacrylamide) is frequently deteriorated by the toxicity of additives and residuals.[17] In comparison, natural macromolecules (*e.g.*, alginate, chitosan, agarose and cellulose) exhibit substantial potential for biocompatible applications because of their high safety, high abundance, excellent biocompatibility and outstanding sustainability.[15] For instance, composite hydrogel electrolytes based on sodium alginate and copolymers have been reported to improve the stability of the Zn anode.[18–21] These composite hydrogel electrolytes showed excellent performance in ionic conductivity, electrochemical stability, mechanical properties, and biocompatibility. Nevertheless, the Zn anode exhibited unsatisfactory reversibility in these composite hydrogel electrolytes. For instance, the Zn‖Zn symmetric cell failed after approximately 200 h when paired with the composite hydrogel electrolyte composed of guar gum, sodium alginate, and ethylene glycol.[19] Therefore, designing hydrogel electrolytes based on natural macromolecules to further improve the reversibility of the Zn anode is highly desired.

Herein, a sustainable composite hydrogel electrolyte was developed by ionically cross-linking the natural macromolecules including iota-carrageenan (IC) and sodium alginate (SA). The composite hydrogel electrolyte exhibited a high ionic conductivity of 5.89×10^{-2} S cm^{-1} and a Zn^{2+} transference number of 0.58, providing fast ion transport kinetics during charge/discharge. Meanwhile, the abundant functional groups of the IC and SA macromolecules formed strong hydrogen bonds with water molecules and coordinated with Zn^{2+}, effectively suppressing the reactivity of water molecules and facilitating reversible Zn plating/stripping. Consequently, the Zn‖Cu asymmetric cell realized reversible Zn plating/stripping over 350 cycles with an improved average Coulombic efficiency (CE) of 98.36%. The Zn‖Zn symmetric cell with the composite hydrogel electrolyte showed a stable cycle life of more than 500 h. More importantly, the Zn‖NVO coin cell achieved more than 800 cycles at 2 A g^{-1} with outstanding electrochemical performance. The Zn‖NVO pouch cell based on the hydrogel electrolyte also showed a high specific capacity of 246.1 mA h g^{-1} at 0.5 A g^{-1} and retained 70.7% of its initial capacity after 150 cycles. The pouch cell worked well at different bending angles and exhibited a capacity retention rate of 98% when recovering from 180°-folding. This composite hydrogel electrolyte may provide new opportunities for designing low-cost, safe, and sustainable electrolytes for flexible and biocompatible ZIBs.

2. Results and discussion

2.1 Preparation and characterization of the composite hydrogel electrolyte

The preparation of the composite hydrogel electrolyte is schematically illustrated in Fig. 1a. Typically, a precursor solution was obtained by mixing 2.5 wt% of IC, 1 wt% of SA, and 1 mg L^{-1} of GO in water *via* a simple ''one-pot'' method. Then, the homogeneous precursor solution was poured into a mold and cooled naturally to form a composite hydrogel (denoted as ISG) without zinc salts, corresponding to the cold-set gelation process shown in Fig. S1 (ESI†). The obtained ISG hydrogel exhibited a typical microporous structure (Fig. S2, ESI†), offering abundant ion transport channels. The following ionic cross-linking process was conducted by immersing the cooled precursor in a 2 M $ZnSO_4$ solution, which ultimately resulted in the formation of the ISG hydrogel electrolyte (denoted as ISGHE).

Fourier transform infrared spectroscopy (FTIR) was performed to investigate the polymerization mechanisms and chemical characteristics of the ISGHE. As shown in Fig. 1b, the OH^- vibration peaks of ISG, IC and SA powders located at 3448 cm^{-1} exhibited no significant shift, indicating that the OH^- groups of the SA and IC molecules were not cross-linked upon mixing.[21] The characteristic peaks at 1620 and 1418 cm^{-1} (Fig. 1b) were attributed to the asymmetric and symmetric stretching vibrations of the COO^- groups on the SA chains, respectively.[22,23] For the ISGHE powder, the asymmetric COO^- stretching peak was blue-shifted to 1636 cm^{-1} and the symmetric stretching peak at 1418 cm^{-1} was diminished due to the Zn^{2+}–COO^- coordination.[24] Meanwhile, the characteristic peak at 1032 cm^{-1}, which can be assigned to the vibration of S═O bonds in IC molecules, was blue-shifted to 1104 cm^{-1} in the ISGHE powder due to the cation bridging effect between Zn^{2+} ions and the functional groups of macromolecules.[25] These results suggested that the cross-linking between IC and SA molecules was primarily achieved through the coordination of Zn^{2+}. Furthermore, the O–H stretching vibration peak of the ISG was shifted from 3448 cm^{-1} in the dry state to 3274 cm^{-1} in the hydrogel state (Fig. 1c). Similar phenomena were observed for the spectra of the ISGHE, in which the O–H stretching vibration peak was centered at 3228 cm^{-1}. This suggested that the free water molecules in the composite hydrogel electrolyte were effectively restrained by the abundant oxygen-containing functional groups in the macromolecules through the formation of hydrogen bonds.[26] This water confinement effect is beneficial in suppressing the reactivity of water molecules.[27] Additionally, the blue shift of the characteristic peaks from 1611 to 1636 cm^{-1} and from 1032 to 1085 cm^{-1} (Fig. 1c) provided strong evidence for the coordination between Zn^{2+} and the functional groups including COO^- and ${OSO_3}^-$, as schematically illustrated in Fig. 1d.

Electrochemical tests were conducted to investigate the performance of the composite hydrogel electrolyte. The ISGHE exhibited a high ionic conductivity of 5.89×10^{-2} S cm^{-1} and a Zn^{2+} transference number of 0.58 in contrast to the liquid electrolyte (denoted as LE) with an ionic conductivity of

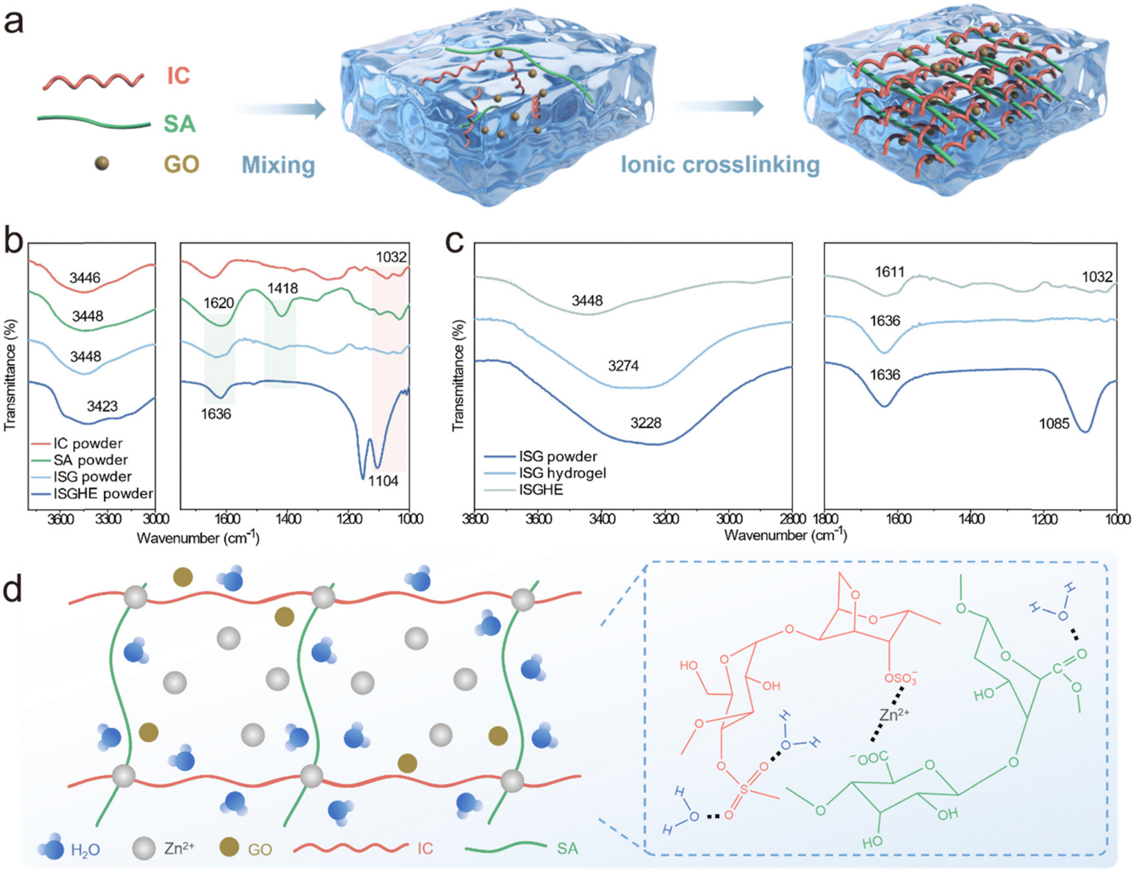

Fig. 1 Fabrication and characterization of the ISGHE. (a) Schematic illustration of the fabrication process of the ISGHE. (b) FTIR spectra of ISG, SA, ISG and ISGHE powders in the dry state. (c) FTIR spectra of the ISG powder, ISG hydrogel and ISGHE. (d) Schematic illustrations of the cross-linking mechanisms.

1.36×10^{-2} S cm^{-1} and a Zn^{2+} transference number of 0.40 (Fig. S3–S5, ESI†). Notably, the hydrogel electrolyte without the introduction of GO (labeled as ISHE) exhibited a lower ionic conductivity of 4.51×10^{-2} S cm^{-1} than the ISGHE, suggesting that the GO acted as an additional dielectric substance and facilitated ion transport in the composite hydrogel electrolyte.[11] In addition, the electrochemical stability window (ESW) of the ISGHE and LE was evaluated by linear scanning voltammetry tests (Fig. S6, ESI†). Compared with the LE, the ESW of the ISGHE was significantly extended due to the anchoring effect on free water molecules. In particular, the onset potential of the hydrogen evolution reaction was shifted from 0.35 V *vs.* Zn^{2+}/Zn for the LE to −0.13 V *vs.* Zn^{2+}/Zn for the ISGHE, signifying the suppression of hydrogen evolution in the presence of IC and SA macromolecules.

2.2 Regulation of Zn nucleation/growth in the ISGHE

The formation of Zn dendrites during the charge/discharge process of ZIBs is a persistent issue, which is closely related to the nucleation and growth behaviors of Zn. To investigate the effect of the ISGHE on Zn nucleation and growth, electrochemical tests were performed to determine the Zn nucleation overpotentials in Zn‖Cu asymmetric cells. As shown in Fig. 2a, the Zn‖Cu asymmetric cell based on the ISGHE showed a nucleation overpotential of 47.4 mV *vs.* Zn^{2+}/Zn, higher than that (37.8 mV *vs.* Zn^{2+}/Zn) of the LE-based cell. The relationship between nucleation overpotential and critical nucleus radius can be described using the following equation:[28]

$$r = \frac{2\gamma V_{\mathrm{m}}}{F|\eta_{\mathrm{n}}|}$$

where γ is the surface energy of the Zn–electrolyte interface, V_{m} is the molar volume of Zn, η_{n} is the deposition overpotential and F is Faraday's constant. Therefore, a larger nucleation overpotential will lead to a smaller critical nucleation radius, which is highly desired to suppress Zn dendrite growth and improve the reversibility of the Zn anode. Furthermore, as shown by the chronoamperometry curves presented in Fig. 2b, the Zn anode exhibited a short two-dimensional (2D) diffusion process of approximately 40 s and achieved a stable current of −0.047 mA cm^{-2} during the three-dimensional (3D) diffusion process when paired with the ISGHE. This indicated the fast and homogeneous Zn nucleation and deposition in the ISGHE, attributing to the regulation effect of macromolecules on Zn^{2+} distribution and migration.[24,29] In comparison, the Zn anode with the LE reached a high current of −0.084 mA cm^{-2} after a long 2D diffusion process due to the "tipping effect" induced by Zn dendrite growth.[30]

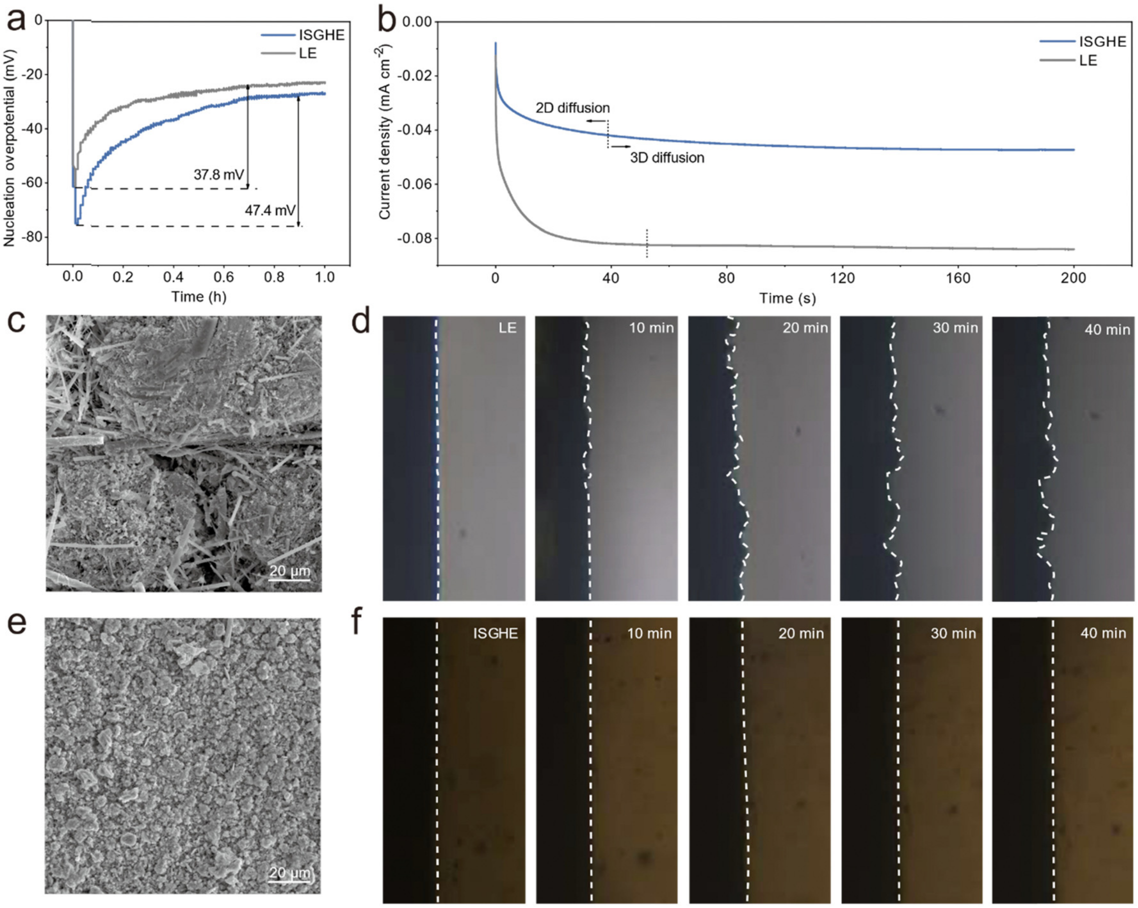

Fig. 2 Nucleation and growth behaviors of Zn in the ISGHE. (a) Nucleation overpotentials obtained from Zn‖Cu asymmetric cells based on the ISGHE and LE. (b) Chronoamperometry tests of Zn‖Zn symmetric cells based on the ISGHE and LE at a constant voltage of −10 mV. (c) SEM image of Zn deposited on Cu foil after 5 h at 2 mA cm^{-2} in the LE. (d) *In situ* optical images of Zn deposits obtained in the LE. (e) SEM image of Zn deposited on Cu foil after 5 h at 2 mA cm^{-2} in the ISGHE. (f) *In situ* optical images of Zn deposits obtained in the ISGHE.

Scanning electron microscopy (SEM) and optical images of Zn deposits were obtained to reveal their morphologies. As shown in Fig. 2c, the Zn deposited in the LE was developed into large aggregates and unevenly distributed on the Cu substrate. Additionally, glass fibers from the separator were embedded into these large Zn aggregates, implying the piercing effect due to fast Zn dendrite growth in the LE.[31] In sharp contrast, the Zn deposits obtained in the ISGHE were uniformly distributed among the substrate with fine grain sizes. These results are in good agreement with the Zn nucleation overpotentials obtained in ISGHE- and LE-based Zn‖Cu cells (Fig. 2a). *In situ* optical microscopy was employed to visualize the evolution of the Zn/electrolyte interface during Zn plating at a current density of 10 mA cm^{-2}. As the plating time increased, the flat Zn/LE interface became uneven with obvious protrusions (Fig. 2d) due to Zn dendrite growth. In contrast, the Zn/ISGHE interface remained flat and uniform during the entire Zn deposition process (Fig. 2f). The effective inhibition of Zn dendrite growth in the ISGHE could be attributed to the homogenized distribution of Zn^{2+} ions at the Zn/electrolyte interface.[32]

2.3 Stability of the Zn anode in the ISGHE

Tafel tests were conducted to investigate the corrosion behaviors of the Zn anode in different electrolytes. The Zn anode in the ISGHE exhibited a lower corrosion current of 0.499 mA cm^{-2} compared to that (1.309 mA cm^{-2}) in the LE (Fig. S7, ESI†), which could be attributed to the suppression of water reactivity by the IC and SA macromolecules. Fig. 3a shows the SEM and elemental mappings of the Zn anode after 10 plating/stripping cycles in a symmetric cell with the ISGHE. The cycled Zn anode displayed a flat and uniform surface morphology when paired with the ISGHE. Comparatively, inhomogeneous Zn deposits and corrosion pits were observed on the Zn surface cycled in the LE (Fig. 3b). Moreover, the elemental mappings indicated that high concentrations of S and O elements were passivated on the surface of the Zn anode cycled in the LE due to the presence of by-products induced by parasitic side reactions. The XRD results shown in Fig. 3c further confirmed that significant amounts of $Zn_4SO_4(OH)_6{\cdot}3H_2O$ (ZHS) by-products were formed on the Zn surface during the cycling process in the LE. The ZHS by-products not only acted as a physical barrier to block Zn^{2+} transport but also continuously consumed aqueous electrolyte

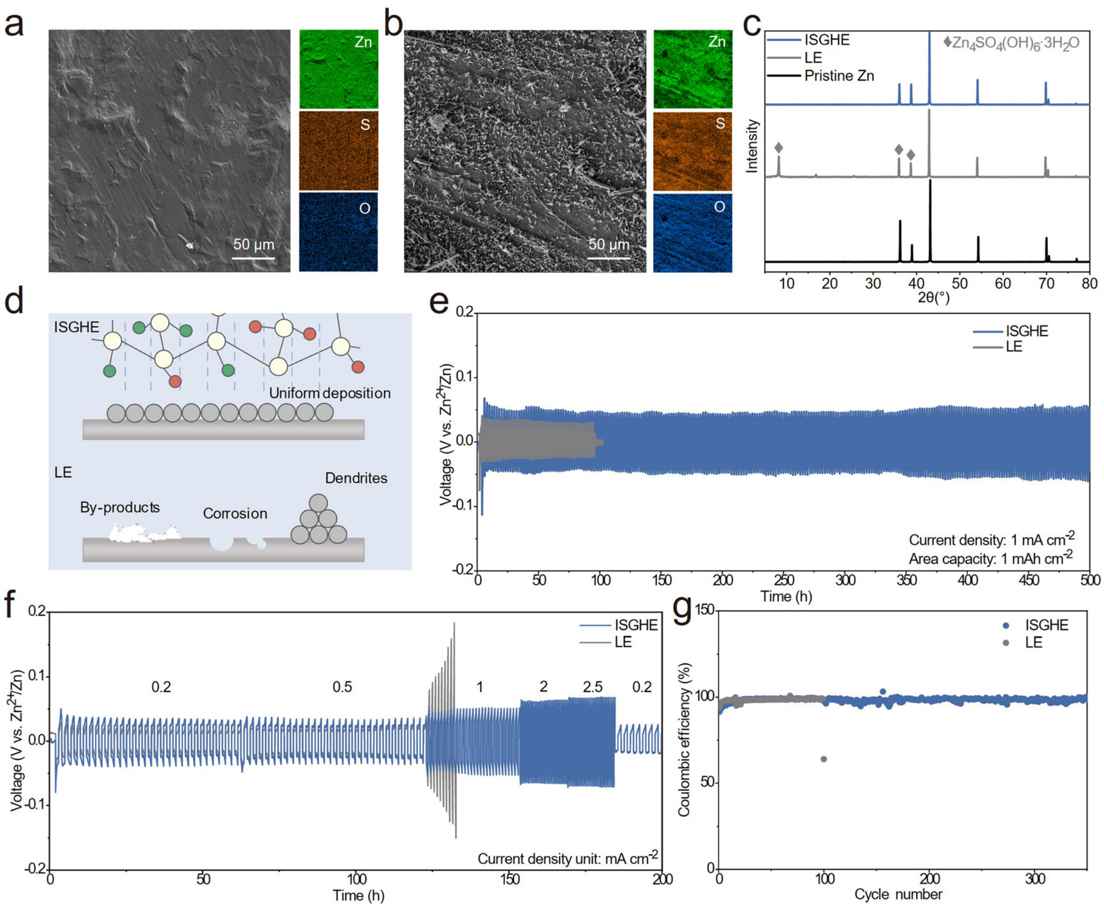

Fig. 3 Anti-corrosion and reversibility of the Zn anode in the ISGHE. SEM images of Zn anodes after 10 cycles in Zn‖Zn symmetric cells based on the (a) ISGHE and (b) LE. (c) XRD patterns of Zn anodes after 10 cycles in Zn‖Zn symmetric cells based on the ISGHE and LE. (d) Schematic illustrations of Zn anodes cycled in the ISGHE and LE. (e) Long-term galvanostatic cycling performance of Zn‖Zn symmetric cells at 1 mA cm^{-2} and 1 mA h cm^{-2} in the ISGHE and LE. (f) Rate performance of Zn‖Zn symmetric cells at different current densities based on the ISGHE and LE. (g) CEs of Zn‖Cu asymmetric cells at 1 mA cm^{-2} and 1 mA h cm^{-2} in the ISGHE and LE.

species, exacerbating the growth of Zn dendrites and the hydrogen evolution reaction.[33] For the Zn anode paired with the ISGHE, no characteristic diffraction peaks corresponding to ZHS by-products were observed (Fig. 3c). These results demonstrated that the ISGHE could effectively suppress water-induced side reactions and thus improve the reversibility of the Zn anode, as schematically illustrated in Fig. 3d.

To further investigate the stability of the Zn anode, Zn‖Zn symmetric cells were assembled and tested. The voltage–time profiles showed that the Zn plating/stripping of the Zn‖Zn symmetric cell with the ISGHE remained stable for more than 500 h at 1 mA cm^{-2} and 1 mA h cm^{-2}, outperforming that (<100 h) of the symmetric cell based on the LE (Fig. 3e). At a higher current density of 5 mA cm^{-2} and a higher areal capacity of 1.25 mA h cm^{-2}, the Zn‖Zn symmetric cell based on the ISGHE also exhibited a longer cycle life compared to that of the LE-based symmetric cell (Fig. S8, ESI†). Furthermore, the ISGHE-based Zn‖Zn symmetric cell exhibited excellent rate capability at different current densities ranging from 0.2 to 2.5 mA cm^{-2} (Fig. 3f). Comparatively, the Zn‖Zn symmetric cell based on the LE failed when the current density was increased to 1 mA cm^{-2} due to short circuits. Fig. 3g shows the CE of the Zn‖Cu asymmetric cells with different electrolytes. The cell with the ISGHE exhibited an average Coulombic efficiency (CE) of 98.36% over 350 cycles, superior to the LE-based Zn‖Cu asymmetric cell with an average CE of 98.13% for less than 100 cycles.

2.4 Electrochemical performance of the Zn‖NVO full cells

To investigate the effectiveness of the ISGHE in practical applications, full cells with the $NH_4V_4O_{10}$ (NVO) cathode were assembled. The NVO cathode was synthesized according to the procedure described in our prior work and the XRD pattern (Fig. S9, ESI†) of the obtained NVO products agreed well with our previous results.[34] Fig. 4a shows the cyclic voltammetry (CV) curves of the Zn‖NVO full cells based on the ISGHE and LE at a scan rate of 0.1 mV s^{-1}. The reduction/oxidation peaks of the two cells coincided well and exhibited the typical Zn^{2+} insertion/extraction characteristics associated with NVO. Moreover, the full cell based on the ISGHE exhibited a higher capacity retention rate of 95.9% after 3 cycles at 0.1 mV s^{-1}, superior to that (93.4%) of the full cell based on the LE

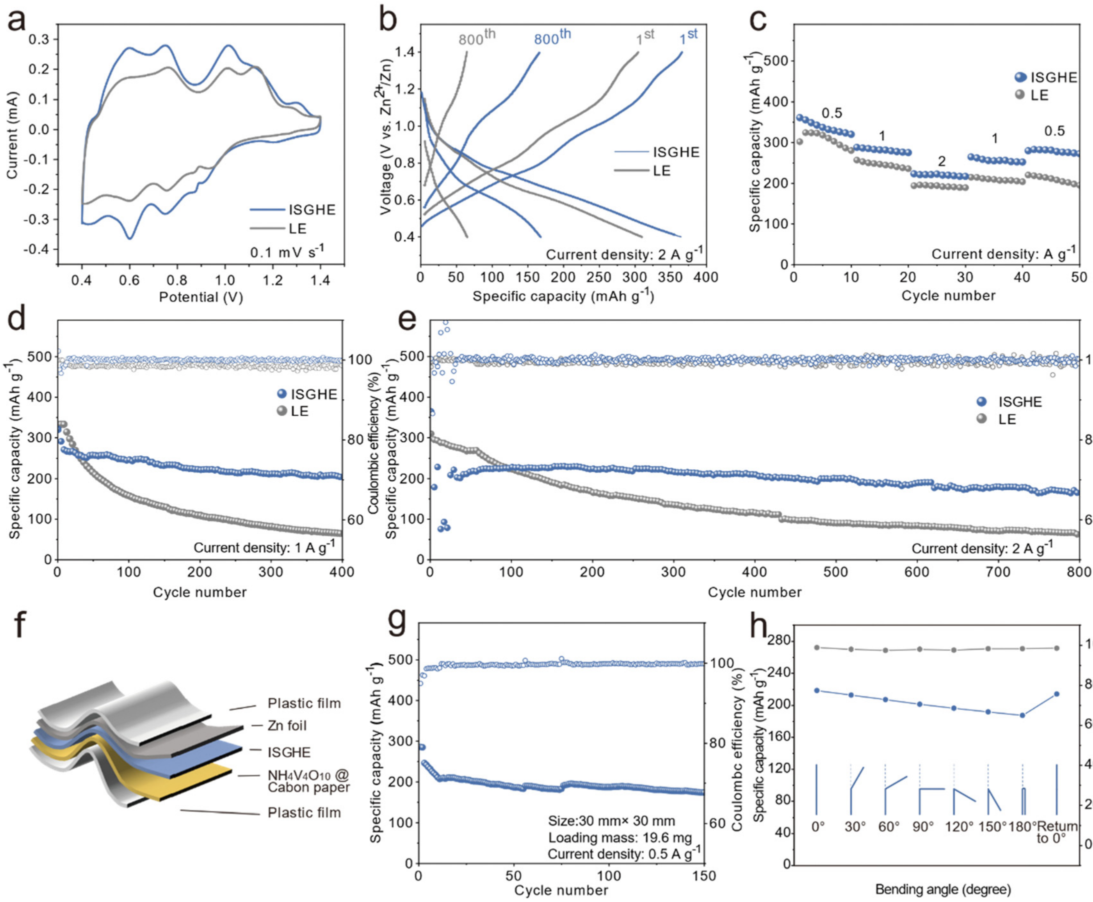

Fig. 4 Electrochemical performance of Zn‖$NH_4V_4O_{10}$ full cells based on the ISGHE and LE. (a) CV plots of Zn‖NVO full cells based on the ISGHE and LE at a scan rate of 0.1 mV s^{-1}. (b) Voltage profiles and (c) rate performance of Zn‖NVO full cells based on the ISGHE and LE. (d) Long-term cycling performance of Zn‖NVO full cells at a current density of 1 A g^{-1}. (e) Long-term cycling performance of Zn‖NVO full cells at a current density of 2 A g^{-1}. (f) Schematic illustration of the pouch cell based on the ISGHE. (g) Long-term cycling performance of the Zn‖NVO pouch cell at a current density of 0.5 A g^{-1}. (h) Folding tests of the ISGHE-based pouch cell at different bending states.

(Fig. S10, ESI†). Fig. 4b shows the charge/discharge curves of the Zn‖NVO full cells at a current density of 2 A g^{-1}. Compared to the full cell based on the LE, the ISGHE-based full cell delivered a noticeably higher capacity over 800 cycles. The results showed that the ISGHE significantly inhibited Zn dendrite growth and water-induced side reactions, thus improving the stability of the batteries. In addition, the ISGHE-based full cell displayed a charge transfer resistance of 141 Ω, which was significantly lower than that (400 Ω) of the full cell with the LE (Fig. S11, ESI†).

Fig. 4c shows the rate performance of the full cells at different current densities ranging from 0.5 to 2 A g^{-1}. The ISGHE-based full cell delivered a discharge capacity of 361 mA h g^{-1} at 0.5 A g^{-1} and retained a discharge capacity of 225 mA h g^{-1} at 2 A g^{-1}, indicating its excellent rate capability at different current densities. Fig. 4d shows the long-term cycling stability of the full cells at 1 A g^{-1}. The full cell based on the ISGHE retained 64.5% of its initial capacity after 400 cycles. For the LE-based full cell, the capacity rapidly decayed under the same testing conditions with a retention rate of 19.1% after 400 cycles due to fast Zn dendrite growth and severe side reactions at the Zn/electrolyte interface. Fig. 4e shows the long-term cycling performance of the full cells over 800 cycles at a higher current density of 2 A g^{-1}. Due to the poor reversibility of the Zn anode, the capacity of the full cell with the LE quickly decayed to 65 mA h g^{-1} after 800 cycles. In contrast, the ISGHE-based battery exhibited a high capacity of approximately 200 mA h g^{-1} after 600 cycles and displayed an outstanding capacity retention rate of 73.6% after 800 cycles. It is worth noting that the specific capacity of the full cell based on the ISHE only reached around 140 mA h g^{-1} at 1 A g^{-1}, significantly lower than that (∼220 mA h g^{-1}) of the ISGHE-based full cell (Fig. S12, ESI†). This agreed well with the ionic conductivities of the ISHE and ISGHE, and the improved ion transportation in the ISGHE resulted in the superior electrochemical performance of the full cells.

Fig. S13 (ESI†) shows the SEM images and elemental mappings of the cycled Zn anodes in the LE- and ISGHE-based full cells. The results showed that the vanadium element formed large aggregates and was more concentrated on the surface of the Zn anode cycled in the LE-based Zn‖NVO full cell. Meanwhile, in the ISGHE, no significant vanadium aggregation was observed and the vanadium was evenly distributed over the surface of the cycled Zn anode. This may be attributed to the inhibition of cathode dissolution and suppression of the shuttling effect by the hydrogel network, which greatly reduced the formation of vanadium-containing by-products on the anode side.[35] The self-discharge performance of full cells based on different electrolytes was investigated by determining the capacity retention rate of fully charged batteries after resting for 60 h. As shown in Fig. S14 (ESI†), the ISGHE-based Zn‖NVO full cell exhibited a high CE of 81.7%. In comparison, the self-discharge was more severe in the full cell based on the LE with a CE of 70.4% due to the proceeding of irreversible side reactions upon resting.

To evaluate the feasibility of the ISGHE in flexible devices, pouch cells were assembled as illustrated in Fig. 4f. The pouch cell exhibited a high initial specific capacity of 246.1 mA h g^{-1} at 0.5 A g^{-1} after activation and displayed a capacity retention rate of 70.7% after 150 cycles (Fig. 4g). The flexibility of the pouch cell was confirmed by folding tests at different angles, as shown in Fig. 4h. The specific capacity of the pouch cell slightly decreased when increasing the folding angles from 0 to 180°. For instance, the specific capacities of the ISGHE-based pouch cell were 218.5 and 187.4 mA h g^{-1} at folding angles of 0 and 180°, respectively. The decreased specific capacity at higher bending angles could be attributed to increased contact resistance between different components of the pouch cell in the folded state. Importantly, the pouch cell retained a capacity of 214.1 mA h g^{-1} after recovering from 180° folding, corresponding to a high capacity retention rate of 98% compared to its initial capacity. The folded pouch cells successfully powered an array of light bulbs (Fig. S15, ESI†), confirming the excellent flexibility of the ISGHE-based ZIBs.

3. Conclusions

In conclusion, a composite hydrogel electrolyte based on natural macromolecules is developed to improve the stability of ZIBs. The ISGHE exhibits a high ionic conductivity of 5.89×10^{-2} S cm^{-1} and an appreciable Zn^{2+} transference number of 0.58. The abundant carboxyl and sulfate groups in the IC and SA macromolecules significantly confine water molecules *via* the formation of hydrogen bonds, thus inhibiting water-induced side reactions and Zn dendrite formation. Consequently, the Zn‖Cu asymmetric cell based on the ISGHE realizes reversible Zn plating/stripping over 350 cycles and the Zn‖Zn symmetric cell remains stable over 500 h at 1 mA cm^{-2} and 1 mA h cm^{-2}. The resulting ISGHE-based full cells also exhibit excellent long-term cycling stability over 400 cycles at 1 A g^{-1} and 800 cycles at 2 A g^{-1}. The ISGHE could also effectively improve the electrochemical performance of the full cells upon resting. Additionally, the pouch cell based on the ISGHE exhibits a high specific capacity of 246.1 mA h g^{-1} at 0.5 A g^{-1} and displays a capacity retention rate of 70.7% after 150 cycles. When returning the folding angles from 180 to 0°, the ISGHE-based pouch cell retains 98% of its initial capacity, demonstrating the excellent flexibility, stability and electrochemical performance of the ISGHE-based ZIBs. This composite hydrogel electrolyte based on natural macromolecules may offer new opportunities for the development of biocompatible and flexible battery technologies.

Data availability

The data that support the findings of this study are available from the corresponding author upon reasonable request.

Conflicts of interest

The authors declare no conflicts of interest.

Acknowledgements

This work was supported by the National Natural Science Foundation of China (Grant No. 52372252 and 52172263) and the Natural Science Foundation of Hunan Province (Grant No. 2022JJ30051).

References

1 G. Fang, J. Zhou, A. Pan and S. Liang, *ACS Energy Lett.*, 2018, **3**, 2480–2501.

2 P. Ruan, S. Liang, B. Lu, H. J. Fan and J. Zhou, *Angew. Chem., Int. Ed.*, 2022, **61**, 2200598.

3 B. Tang, L. Shan, S. Liang and J. Zhou, *Energy Environ. Sci.*, 2019, **12**, 3288–3304.

4 W. Yang, Y. Yang, H. Yang and H. Zhou, *ACS Energy Lett.*, 2022, **7**, 2515–2530.

5 X. Li, Z. Chen, P. Ruan, X. Hu, B. Lu, X. Yuan, S. Tian and J. J. N. Zhou, *Nanoscale*, 2024, **16**, 2923.

6 J. Li, Z. Liu, S. Han, P. Zhou, B. Lu, J. Zhou, Z. Zeng, Z. Chen and J. Zhou, *Nano-Micro Lett.*, 2023, **15**, 237.

7 Y. Hu, Z. Liu, L. Li, S. Guo, X. Xie, Z. Luo, G. Fang and S. Liang, *Natl. Sci. Rev.*, 2023, **10**, nwad220.

8 Y. Zhong, X. Xie, Z. Zeng, B. Lu, G. Chen and J. Zhou, *Angew. Chem., Int. Ed.*, 2023, **62**, 2310577.

9 L. Suo, O. Borodin, T. Gao, M. Olguin, J. Ho, X. Fan, C. Luo, C. Wang and K. Xu, *Science*, 2015, **350**, 938–943.

10 S. Lei, Z. Liu, C. Liu, J. Li, B. Lu, S. Liang and J. Zhou, *Energy Environ. Sci.*, 2022, **15**, 4911–4927.

11 X. Xiao, X. Xiao, Y. Zhou, X. Zhao, G. Chen, Z. Liu, Z. Wang, C. Lu, M. Hu, A. Nashalian, S. Shen, K. Xie, W. Yang, Y. Gong, W. Ding, P. Servati, C. Han, S. X. Dou, W. Li and J. Chen, *Sci. Adv.*, 2021, **7**, eabl3742.

12 H. Li, C. Han, Y. Huang, Y. Huang, M. Zhu, Z. Pei, Q. Xue, Z. Wang, Z. Liu, Z. Tang, Y. Wang, F. Kang, B. Li and C. Zhi, *Energy Environ. Sci.*, 2018, **11**, 941–951.

13 X. Xie, J. Li, Z. Xing, B. Lu, S. Liang and J. Zhou, *Natl. Sci. Rev.*, 2022, **10**, nwac281.

14 Y. Wang, Q. Li, H. Hong, S. Yang, R. Zhang, X. Wang, X. Jin, B. Xiong, S. Bai and C. Zhi, *Nat. Commun.*, 2023, **14**, 3890.

15 H. Ge, X. Xie, X. Xie, B. Zhang, S. Li, S. Liang, B. Lu and J. Zhou, *Energy Environ. Sci.*, 2024, **17**, 3270–3306.

16 Z. Wang, H. Li, Z. Tang, Z. Liu, Z. Ruan, L. Ma, Q. Yang, D. Wang and C. Zhi, *Adv. Funct. Mater.*, 2018, **28**, 1804560.

17 W. Deng, Z. Zhou, Y. Li, M. Zhang, X. Yuan, J. Hu, Z. Li, C. Li and R. Li, *ACS Nano*, 2020, **14**, 15776–15785.

18 Y. Lu, T. Zhu, N. Xu and K. Huang, *ACS Appl. Energy Mater.*, 2019, **2**, 6904–6910.

19 J. Wang, Y. Huang, B. Liu, Z. Li, J. Zhang, G. Yang, P. Hiralal, S. Jin and H. Zhou, *Energy Storage Mater.*, 2021, **41**, 599–605.

20 H. Dong, J. Li, S. Zhao, Y. Jiao, J. Chen, Y. Tan, D. J. L. Brett, G. He and I. P. Parkin, *ACS Appl. Mater. Interfaces*, 2021, **13**, 745–754.

21 B. Zhang, L. Qin, Y. Fang, Y. Chai, X. Xie, B. Lu, S. Liang and J. Zhou, *Sci. Bull.*, 2022, **67**, 955–962.

22 M. O. Taha, W. Nasser, A. Ardakani and H. S. AlKhatib, *Int. J. Pharm.*, 2008, **350**, 291–300.

23 J. Mirtič, J. Ilaš and J. Kristl, *Carbohydr. Polym.*, 2018, **181**, 93–102.

24 Y. Tang, C. Liu, H. Zhu, X. Xie, J. Gao, C. Deng, M. Han, S. Liang and J. Zhou, *Energy Storage Mater.*, 2020, **27**, 109–116.

25 J. Prado-Fernández, J. Rodrıguez-Vázquez, E. Tojo and J. J. A. C. A. Andrade, *Anal. Chim. Acta*, 2003, **480**, 23–37.

26 S. Chen, S. Ding, Q. Chen and J. Zhang, *Chem. Sci.*, 2022, **14**, 331–337.

27 P. Wang, S. Liang, C. Chen, X. Xie, J. Chen, Z. Liu, Y. Tang, B. Lu and J. Zhou, *Adv. Mater.*, 2022, **34**, 2202733.

28 A. Pei, G. Zheng, F. Shi, Y. Li and Y. Cui, *Nano Lett.*, 2017, **17**, 1132–1139.

29 C. Y. Chan, Z. Wang, Y. Li, H. Yu, B. Fei and J. H. Xin, *ACS Appl. Mater. Interfaces*, 2021, **13**, 30594–30602.

30 X. Xie, S. Liang, J. Gao, S. Guo, J. Guo, C. Wang, G. Xu, X. Wu, G. Chen and J. Zhou, *Energy Environ. Sci.*, 2020, **13**, 503–510.

31 S. Tian, T. Hwang, Y. Tian, Y. Zhou, L. Zhou, T. Milazzo, S. Moon, S. Malakpour Estalaki, S. Wu, R. Jian, K. Balkus, T. Luo, K. Cho and G. Xiong, *ACS Nano*, 2023, **17**, 14930–14942.

32 Y. Hao, D. Feng, L. Hou, T. Li, Y. Jiao and P. Wu, *Adv. Sci.*, 2022, **9**, 2104832.

33 W. Zhang, Y. Dai, R. Chen, Z. Xu, J. Li, W. Zong, H. Li, Z. Li, Z. Zhang, J. Zhu, F. Guo, X. Gao, Z. Du, J. Chen, T. Wang, G. He and I. P. Parkin, *Angew. Chem., Int. Ed.*, 2023, **62**, 2212695.

34 Y. Fang, X. Xie, B. Zhang, Y. Chai, B. Lu, M. Liu, J. Zhou and S. Liang, *Adv. Funct. Mater.*, 2022, **32**, 2109671.

35 Z. Xing, G. Xu, X. Xie, M. Chen, B. Lu, J. Zhou and S. Liang, *Nano Energy*, 2021, **90**, 106621.